JOURNAL OF MODERN OPTICS, 1997, VOL. 44, NO. 11/12, 2485–2505

Experimental preparation and measurement of quantum states of motion of a trapped atom †

D. LEIBFRIED, D. M. MEEKHOF, C. MONROE, B. E. KING, W. M. ITANO and D. J. WINELAND

Time and Frequency Division, National Institute of Standards and Technology, 325 Broadway, Boulder, CO 80303-3328, USA

(*Received 5 November 1996*)

Abstract. We report the creation and full determination of several quantum states of motion of a $^9Be^+$ ion bound in a RF (Paul) trap. The states are coherently prepared from an ion which has been initially laser cooled to the zero-point of motion. We create states having both classical and non-classical character including thermal, number, coherent, squeezed, and 'Schrödinger cat' states. The motional quantum state is fully reconstructed using two novel schemes that determine the density matrix in the number state basis or the Wigner function. Our techniques allow well controlled experiments decoherence and related phenomena on the quantum–classical borderline.

1. Introduction

The ability to create and completely characterize a variety of fundamental quantum states has long been sought after in the laboratory since it brings to the forefront issues involving the relationship between quantum and classical physics. Since most theoretical proposals to achieve these goals were put forward in the field of quantum optics, it might seem surprising that some of the first experiments succeeding in both respects were realized on the motion of a trapped atom. However, since both the photon field of quantum optics and the motion of a trapped atom are quantum harmonic oscillators, their couplings to internal atomic levels (described by the Jaynes–Cummings model (JCM) [1, 2]) are quite similar [3, 4]. In addition, for the case of a harmonically-bound atom driven by a light field, there are interactions beyond the simple Jaynes–Cummings coupling, allowing more control over the engineering and measurement of quantum states.

Section 2 will give a brief description of the interaction of a trapped atom with light fields and outline the similarities to the Jaynes–Cummings Hamiltonian studied in quantum optics. Our experimental setup and the cooling of the trapped atom to the motional ground state are described in section 3. We then describe the controlled preparation of both classical and non-classical motional states including a 'Schrödinger-cat' type state in section 4. The complete measurement of either the density matrix in the number state basis or the Wigner function is covered in section 5 and we finally offer some conclusions in section 6.

† Work of the U.S. Government. Not subject to U.S. copyright.

0950–0340/97 $12·00 © 1997 Taylor & Francis Ltd.

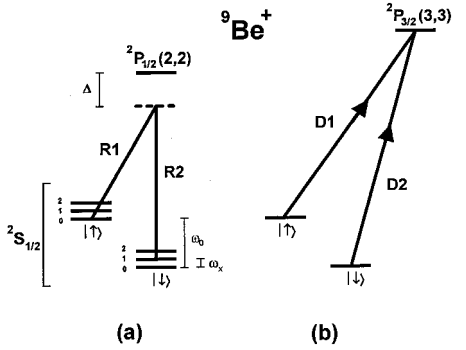

Figure 1. (*a*) Electronic (internal) and motional (external) energy levels of the trapped Be^+ ion, coupled by laser beams R1 and R2. The difference frequency of the Raman beams is set near $\omega_0/2\pi \simeq 1{\cdot}250\,\mathrm{GHz}$, providing a two photon Raman coupling between the $^2S_{1/2}(F = 2, m_F = 2)$ and $^2S_{1/2}(F = 1, m_F = 1)$ hyperfine ground states (denoted by $|\downarrow\rangle$ and $|\uparrow\rangle$ respectively). The motional energy levels are depicted by a ladder of vibrational states separated by the trap frequency $\omega_x/(2\pi) \simeq 11{\cdot}2\,\mathrm{MHz}$. The Raman beams are detuned by $\Delta/(2\pi) \simeq -12\,\mathrm{GHz}$ from the $^2P_{1/2}$ ($F = 2$, $m_F = 2$) excited state. As shown, the Raman beams are tuned to the first red sideband. (*b*) Detection of the internal state is accomplished by illuminating the ion with a σ^+ polarized 'detection' beam D2, which drives the cycling $^2S_{1/2}$ ($F = 2$, $m_F = 2$) $\rightarrow$ $^2P_{3/2}(F = 3, \ m_F = 3)$ transition, and observing the scattered fluorescence. The vibrational structure is omitted from (*b*) since it is not resolved. Beam D1, also σ^+ polarized, provides spontaneous recycling from the $|\uparrow\rangle$ to $|\downarrow\rangle$ state.

2. Interaction of a trapped atom with light fields

To describe the interaction of the trapped atom with light fields we make the following assumptions which will be justified below. First we assume that the internal degrees of freedom of the trapped atom are sufficiently described by a two level system, second that the motion of the atom bound in the trap is harmonic in all three dimensions, and finally that the vibrational level spacings (trap frequencies) and internal state transition frequencies are much larger than any internal or motional relaxation rates. Starting from these assumptions we can describe the trapped atom as a two level system with levels labeled $|\downarrow\rangle$, and $|\uparrow\rangle$, dressed by the harmonic oscillator ladders of the external motion with number states $|n_x n_y n_z\rangle$. We will consider coupling to only the $\hat{x}$ dimension harmonic oscillator with number states $|n_x\rangle = |n\rangle$ [$n = 1, 2, \ldots \infty$, see figure 1 (*a*)]. To couple the motional and internal degrees of freedom of the trapped atom, we apply two laser beams whose difference frequency matches the separation of two energy levels, as depicted in figure 1 (*a*). The beams are each sufficiently detuned from short-lived excited electronic states, resulting in two-photon stimulated Raman transitions between the states of interest which are formally equivalent to narrow single photon transitions. By employing two laser beams to drive stimulated Raman transitions, we are able to combine the advantages of strong optical electric-field gradients (allowing manipulation of the state of motion) and microwave stability of the crucial difference frequency.

In the rotating wave approximation in a frame rotating with ω_0, where $\hbar\omega_0$ is the energy difference of the two internal levels, the interaction of the classical laser field with the two levels of the trapped atom is described by the Hamiltonian

$$H_{\mathrm{int}}(t) = \hbar g(\sigma_+ \exp\left[-i(\delta t - \mathbf{k}\cdot\mathbf{x})\right] + \sigma_- \exp\left[i(\delta t - \mathbf{k}\cdot\mathbf{x}\right], \qquad (1)$$

where g denotes the interaction strength, σ^+ and σ^- are the Pauli spin matrices describing the two level system and δ the detuning of the frequency difference of the two Raman beams $\omega = \omega_1 - \omega_2$ with respect to ω_0, and $\mathbf{k} = \mathbf{k}_1 - \mathbf{k}_2$ is the difference of the two Raman beam wave-vectors. In these experiments the wave-vector difference was always chosen to be parallel with the $\hat{x}$-direction of the trap, so $\mathbf{k}\cdot\mathbf{x} = kx$ and the interaction couples only the motion in $\hat{x}$-direction to the internal state of the trapped atom.

In our experiment we confine a single beryllium-ion in a RF-(Paul) trap [5], so the trapping potential is not a simple harmonic potential but rather a time dependent potential with the periodicity of the RF field. Based on the full quantum mechanical treatment of Glauber [6], several workers have studied the time dependence of the interaction Hamiltonian (1) [7, 8]. While Bardroff *et al.* [7] give a general expression for the Rabi frequencies, we restrict ourselves to an approximate treatment in the limit where the dimensionless Paul trap parameters a and q related to the static and RF-potential [5] are much smaller than one (in our trap, $a \simeq 0$, $q \simeq 0{\cdot}14$). The main change in the full treatment is a common scaling factor in the interaction strength (Rabi frequencies). This is already taken into account in our experiments, since we scale all our Rabi frequencies with the experimentally determined Rabi frequency $\Omega_{0,1}$ (see below). In the approximation of a simple harmonic oscillator, with creation and destruction operators a^+ and a, the interaction Hamiltonian (1) reduces to

$$H_{\text{eff}} = \hbar g(\sigma_+ \exp\left[i\eta(a^\dagger + a) - i\delta t\right] + \sigma_- \exp\left[-\eta(a^\dagger + a) + i\delta t\right], \tag{2}$$

where $\eta = k\left[\hbar/(2m\omega_x)\right]^{1/2}$, m is the mass and ω_x is the secular frequency of the ion in $\hat{x}$-direction. By tuning the frequency difference δ to an integer multiple of the secular frequency ω_z, $\delta = (n' - n)\omega_z$, we can resonantly drive transitions from $|\downarrow, n\rangle$ to $|\uparrow, n'\rangle$. In this case H_{eff} is dominated by a single stationary term. The exponent $\exp\left[i\eta(a^\dagger + a)\right]$ in H_{eff} contains all powers of a and $a^\dagger$. Since their time dependence (in the interaction picture) is $a(t)^m = \tilde{a}(t)^m \exp(-im\omega_x t)$, all contributions with $m \neq n' - n$ oscillate rapidly and average out when ω_x is much larger than g. The biggest stationary term in the Lamb–Dicke limit ($\langle\eta(a + a^\dagger)^2\rangle^{1/2} \ll 1$) is proportional to

$$\bar{H}_{\text{eff}} \sim \hbar g \frac{\eta^{n'-n}}{(n'-n)!}(\sigma_+ (a^\dagger)^{n'-n} + \sigma_- a^{n'-n}), \tag{3}$$

if $n' - n > 0$, and

$$\bar{H}_{\text{eff}} \sim \hbar g \frac{\eta^{n-n'}}{(n-n')!}(\sigma_+ a^{n-n'} + \sigma_- (a^\dagger)^{n-n'}), \tag{4}$$

if $n' - n < 0$. In the special case of $n' - n = -1$ ($\delta < 0$, first red sideband) we obtain the familiar Jaynes–Cummings Hamiltonian $\eta(\sigma_+ a + \sigma_- a^\dagger)$. By choosing other detunings we can realize a number of couplings beyond the Jaynes–Cummings coupling; for example a 'two-phonon' coupling $(\eta^2/2)(\sigma_+ a^2 + \sigma_- (a^\dagger)^2)$ for $n - n' = -2$ (second red sideband). The coupling strength to lowest order in η is given by the matrix elements (Rabi frequencies)

$$\hbar\Omega_{n,n'} = \langle\downarrow, n|\bar{H}_{\text{eff}}|\uparrow, n'\rangle \simeq \hbar g \frac{\eta^{|n'-n|}}{|n'-n|}\left[n_>(n_> - 1)\ldots(n_< + 1)\right]^{\frac{1}{2}}, \tag{5}$$

where $n_>$ ($n_<$) is the greater (lesser) of n and n'. The differences are only significant for large n or n'. A 'Rabi-π-pulse', which transfers a pure $|\downarrow, n\rangle$ state to a pure $|\uparrow, n'\rangle$ state, corresponds to applying the Raman beams for a time τ, such that $\Omega_{n,n'}\tau = \pi/2$.

3. Experimental setup and cooling to the motional ground state

In our experiment, a single $^9Be^+$ ion is stored in a RF Paul trap [9] with a secular frequency along x of $\omega_x/2\pi \approx 11{\cdot}2$ MHz, providing a spread of the ground state wavefunction of about $\Delta x_0 \equiv \langle x^2\rangle^{1/2} \approx 7$ nm. The $|\downarrow\rangle$ and $|\uparrow\rangle$ levels are the long-lived $^2S_{1/2}(F = 2, m_F = 2)$ and $^2S_{1/2}(F = 1, m_F = 1)$ hyperfine ground states (see figure 1).

To prepare the ion in the ground state, it is first 'Doppler pre-cooled' by two beams of σ^+ polarized light detuned by approximately one linewidth ($\Gamma/2\pi = 19{\cdot}4$ MHz) to the red of the $^2S_{1/2}(F = 1$ and $2) \rightarrow {}^2P_{3/2}$ transitions. This cools the ion to $\bar{n} \approx 1$, in the $|\downarrow\rangle$ state. To further cool the ion we use narrower Raman transitions in order to be in the resolved sideband limit. One cooling cycle consists of two steps. First we drive stimulated Raman transitions to the $|\uparrow\rangle$ state by applying a pair of travelling-wave laser beams detuned from the $^2P_{1/2}$ state [10]. These Raman beam wave-vectors point at 45° to the $\hat{x}$-axis with their wave-vector difference nearly along the $\hat{x}$-axis of the trap [$\eta_x = 0{\cdot}202(5)$], so the raman transitions are highly insensitive to motion in the $\hat{y}$ or $\hat{z}$ directions. The beams are derived from the same laser with an acousto-optic modulator, reducing the effects of laser frequency jitter. The difference frequency can be tuned near the ground state hyperfine splitting of $\omega_0/2\pi \approx 1{\cdot}25$ GHz. The beams are detuned by approximately 12 GHz to the red of the $^2P_{1/2}$ excited state with approximately 0·5 mW in each beam, so that the Raman transition Rabi frequency $\Omega_{0,1}/2\pi$ is approximately 200 kHz, and the vibrational structure is clearly resolved. For cooling, the frequency difference is tuned to the red sideband ($\delta = -\omega_x$), so that one vibrational quantum is lost in the transfer to the $|\uparrow\rangle$ state. The time during which we apply the red-sideband interaction is optimized to leave the internal state as close to a pure $|\uparrow\rangle$ state as possible (Rabi-π-pulse). In the second step of the cooling cycle, we apply lasers tuned to the $|\uparrow\rangle \rightarrow {}^2P_{3/2}$ and $^2S_{1/2}(F = 2, m_F = 1) \rightarrow {}^2P_{1/2}$ that repump the atom to the $|\downarrow\rangle$ state. In analogy to the Mössbauer effect, the recoil of the spontaneous emission process in this repumping is absorbed by the whole trap structure with high probability, leaving the motional state of the trapped atom unchanged. Five cycles of this two-step cooling scheme prepare the ion in the $|\downarrow, n = 0\rangle$ state approximately 95% of the time [10].

In the experiments described below we detect the probability of being in one of the states $|\uparrow\rangle$ or $|\downarrow\rangle$. We detect $P_\downarrow$, the probability of finding the $|\downarrow\rangle$-state, by driving a cycling transition to the $^2P_{3/2}$ with σ^+ polarized light and detecting the emitted fluorescence. The $|\uparrow\rangle$ is not resonantly coupled to an excited state by the light-field, so $P_\downarrow$ is proportional to the number of tries where we see fluorescence when we repeat the experiment. Since the application of the resonant light field effectively reduces the internal state to either $|\uparrow\rangle$ or $|\downarrow\rangle$, we can consider the internal atomic state to be a unit efficiency detector, even if we fail to detect the fluorescence every time. The analogy with photon detection would be a 100% efficient detector which is read out only sporadically.

4. Creation of various motional states and measurement of their number state population

4.1. *Fock states*

A Fock state $|n\rangle$ is a harmonic oscillator energy eigenstate, designated by the number n of energy quanta. Several techniques for the creation of Fock states of motion have been proposed, using quantum jumps [4, 11], adiabatic passage [12], or trapping states [13]; here we use an alternate technique. Since the ion is initially cooled to the $|\downarrow, 0\rangle$ Fock state, we create higher-n Fock states by simply applying a sequence of Rabi-π-pulses of laser radiation on the blue sideband, red sideband, or carrier. For example, the $|\uparrow, 2\rangle$ state is prepared by using blue sideband, red sideband, and carrier π-pulses in succession, so that the ion steps through the states $|\downarrow, 0\rangle$, $|\uparrow, 1\rangle$, $|\downarrow, 2\rangle$, and $|\uparrow, 2\rangle$ [14].

Once the Fock state is created, the signature of the state can be found by driving Rabi transitions on the blue sideband. Specifically, the Raman beams were tuned to the first blue sideband and applied for a time t. The probability of finding the $|\downarrow\rangle$ level was then measured by applying σ^+ polarized radiation on the $|\downarrow\rangle \rightarrow {}^2P_{3/2}$ cycling transition and detecting the fluorescence as described above. The value of t was stepped, and the data $P\uparrow(t)$ was acquired. The rate of the Rabi flopping, $\Omega_{n,n+1}$ in equation (5), depends on the value of n of the Fock state occupied. The expected signal is

$$P\downarrow(t) = \tfrac{1}{2}\left[1 + \cos(2\Omega_{n,n+1}t)\exp(-\gamma_n(t)\right], \tag{6}$$

where γ_n is the decoherence rate between levels $|n\rangle$ and $|n+1\rangle$. The measured $P\downarrow(t)$ for an initial $|\downarrow, n = 0\rangle$ Fock state is shown in figure 2(*a*) together with a fit to equation (6), yielding $\Omega_{0,1}/(2\pi) = 94(1)$kHz and $\gamma_0 = 11{\cdot}9(4)\ 10^3\ s^{-1}$.

We created a series of Fock states $|\downarrow, n\rangle$ and recorded $P\downarrow(t)$. The measured Rabi frequency ratios $\Omega_{n,n+1}/\Omega_{0,1}$ are plotted in figure 2(*b*), showing very good agreement with the theoretical frequencies corrected for the trap's finite Lamb–Dicke parameter $\eta = 0{\cdot}202$. The observed increase of γ_n with n (we experimentally find $\gamma_n \approx \gamma_0(n+1)^{0.7}$) is qualitatively consistent with our view that the decoherence is due to technical problems.

4.2. *Thermal states*

When the ion's motion is not in a Fock state, $P\downarrow(t)$ shows a more complicated structure. In this case,

$$P\downarrow(t) = \tfrac{1}{2}\left[1 + \sum_{n=0}^{\infty} P_n \cos(2\Omega_{n,n+1}t)\exp(-\gamma_n t)\right], \tag{7}$$

where P_n is the probability of finding the atom in the nth motional number state. For example, a thermal distribution is found after Doppler cooling [15]. In this case, the probability of occupying the nth Fock level is $P_n = \left[\bar{n}^n/(1+\bar{n})^{n+1}\right]$, where $\bar{n}$ is the average vibrational quantum number. The value of $\bar{n}$ can be controlled by the detuning during Doppler cooling. An example of $P\downarrow(t)$ data for a thermal state of motion is given in figure 3. To demonstrate consistency with a thermal state of motion, the time-domain data are fitted to equation (7) with a thermal population distribution for P_n. The signal scale and $\bar{n}$ are allowed to vary in the fit. Values for the base Rabi frequency $\Omega_{0,1}$ and base decay rate γ_0 (from which the other rates are scaled using the dependence found in the Fock state data) are obtained from a

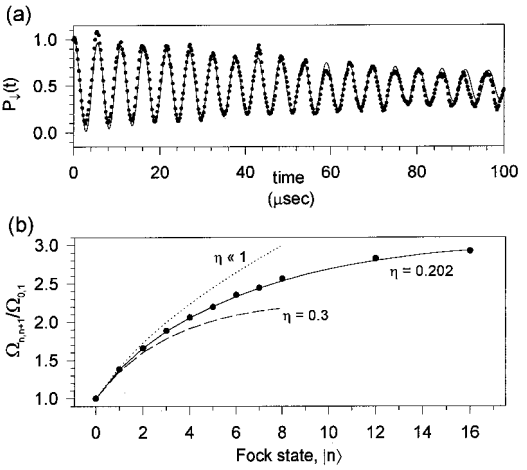

Figure 2. (*a*) $P\downarrow(t)$ for an initial $|\downarrow, 0\rangle$ Fock state driven by a JCM-type interaction provided by tuning the stimulated Raman beams to the first blue sideband. The solid line is a fit to an exponentially decaying sinusoid. 9*b*) The relative Rabi frequencies $\Omega_{n,n+1}/\Omega_{0,1}$ plotted against the prepared Fock state number *n*. The lines represent the predictions of the nonlinear JCM for certain Lamb–Dicke parameters, showing every good agreement with the known Lamb–Dicke parameter $\eta = 0{\cdot}202(5)$. For $\eta \ll 1$ the ratio of the Rabi frequencies is given by $\Omega_{n,n+1}/\Omega_{0,1} = (n+1)^{\frac{1}{2}}$.

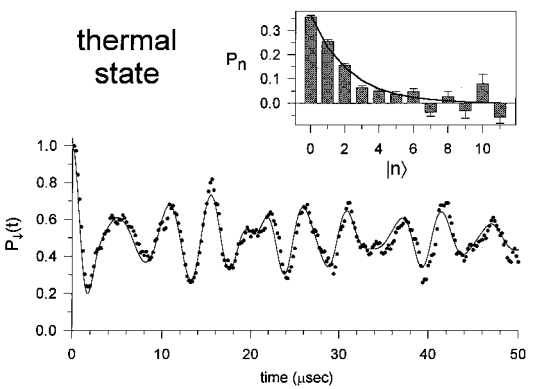

Figure 3. $P\downarrow(t)$ for a thermal state. The data (points) are fitted (line) to a superposition of Fock states with P_n given by a thermal state distribution. The fit allows $\bar{n}$ to vary, yielding a value of $1{\cdot}3 \pm 0{\cdot}1$. The inset shows the decompostion of the data onto the Fock state components (bars) with a fit (line) to the expected exponential distribution, yielding $1{\cdot}5 \pm 0{\cdot}1$.

separate trace of $P\downarrow(t)$ for an initial $|\downarrow, 0\rangle$ state. For figure 3, the fit yields $\bar{n} = 1{\cdot}3 \pm 0{\cdot}1$. The inset shows the results of an independent analysis (the frequency domain analysis). In this case, we directly extract the populations of the various $|n\rangle$ levels. Since the Fock state parameters $\Omega_{n,n+1}$ and γ_n are well characterized, the time-domain data can be decomposed into Fock-state components. Equation (7) is linear in P_n, so we use singular value decomposition [16] to

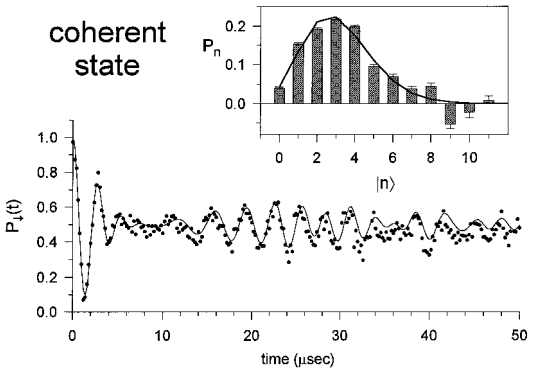

Figure 4. $P\downarrow(t)$ for a coherent state, showing collapse and revival. The data are fitted to a coherent state distribution, yielding $\bar{n} = 3{\cdot}1 \pm 0{\cdot}1$. The inset shows the decomposition of the data onto the expected Fock state components, fitted to a Poissonian distribution, yielding $\bar{n} = 2{\cdot}9 \pm 0{\cdot}1$.

extract the probabilities, shown in the inset of figure 3. The probabilities are fitted to an exponential, yielding $\bar{n} = 1{\cdot}5 \pm 0{\cdot}1$. A third measure of $\bar{n}$ by comparing the size of the red and blue sidebands [10] yields $\bar{n} = 1{\cdot}5 \pm 0{\cdot}2$.

4.3. *Coherent states*

A coherent state of motion $|\alpha\rangle$ of the ion corresponds to a minimum uncertainty wave-packet whose centre oscillates classically in the harmonic well and retains its shape. The probability distribution among Fock states is Poissonian, $P_n = |\langle n \mid \alpha\rangle|^2 = (\bar{n}^n \exp(-\bar{n}))/n!$ with $\bar{n} = |\alpha|^2$. As predicted by the JCM, the internal state evolution $P\downarrow(t)$ will undergo collapses and revivals [17], a purely quantum effect [2, 17].

Coherent states of motion can be produced from the $|n = 0\rangle$ state by a spatially uniform classical driving field [18], by a 'moving standing wave' [19] by pairs of standing waves [20], or by a non-adiabatic shift of the trap centre [21]. We have used the first two methods. For the classical drive, we apply a sinusoidally varying potential at the trap oscillation frequency on one of the trap compensation electrodes [9] for a fixed time (typically 10 μs.) For the 'moving standing wave' creation we use two Raman beams which have a frequency difference of only ω_x. Applying these beams couples adjacent oscillator levels within a given internal state. In the Lamb–Dicke limit this interaction is formally equivalent to applying the coherent displacement operator to the state of motion. The Raman beams produce an optical dipole force which is modulated at ω_x [19], resonantly driving the motion of the atom. On resonance, the magnitude of the coherent state grows linearly with the coupling time.

In figure 4 we present an example of $P\downarrow(t)$ after creation of a coherent state of motion. Similar behaviour has recently been seen in the context of cavity QED [22]. The time domain data are fitted to equation (7) using a Poissonian distribution and allowing only $\bar{n}$ to vary. All other parameters (signal amplitude, signal offset and decoherence rate) are measured from a separate $|n = 0\rangle$ Fock state trace. The inset shows the probabilities of the Fock components, extracted using the frequency domain analysis described above. The amplitudes display the expected Poissonian dependence on n. The observed revival for higher $\bar{n}$ coherent states is

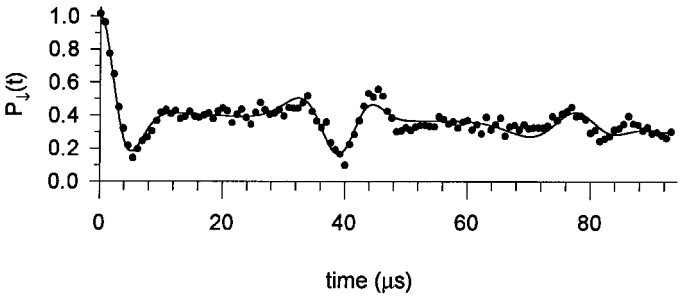

Figure 5. $P_{\downarrow}(t)$ for a coherent state, driven on the second blue sideband. Since the Rabi frequencies are almost commensurate in this interaction, $P_{\downarrow}$ shows very sharp collapse and revival features. The solid line is a fit using the exact Rabi frequencies for finite η It yields $\bar{n} = 2{\cdot}0 \pm 0{\cdot}1$.

attenuated due to the progressively faster decay rates of the higher-n Fock states, and for states with $\bar{n} \gtrsim 7$ we are unable to see the revival.

We can also realize a different interaction by tuning the frequency difference of the Raman beams to the second blue sideband: $\delta = 2\omega_x$. The interaction Hamilton is then proportional to $(\eta^2/2)(\sigma_+(a^\dagger)^2 + \sigma_- a^2)$ [see equation (3)] and the Rabi frequencies [see equation (5)] are given by

$$\Omega_{n,n+2} \simeq g\frac{\eta^2}{2}\left[(n+1)(n+2)\right]^{\frac{1}{2}} \simeq g\frac{\eta^2}{2}(n+\tfrac{3}{2}). \tag{8}$$

Since the last relation holds within 6%for all n, the Rabi frequencies in $P_{\downarrow}(t)$ are almost commensurate, so $P_{\downarrow}(t)$ shows very sharp collapse and revival features, similar to the two-photon cases discussed by Buck and Sukumar [23] and Knight [24]. Our experimental result is shown in figure 5. The factor $\frac{3}{2}$ in the above approximation leads to an additional 3π phase shift between successive revivals. This inverts the interference feature from revival to revival. In addition there are small deviations from equation (8), because of the approximation made and the finite Lamb–Dicke parameter ηwhich alters the Rabi frequencies [see figure 2(*b*)].

4.4. *Squeezed states*

A 'vacuum squeezed state' of motion can be created by a parametric drive [21], by a combination of standing- and traveling-wave laser fields [20], or by a non-adiabatic drop in the trap spring constant [21]. Here we irradiate the $|n = 0\rangle$ ion with two Raman beams which differ in frequency by 2ω, driving Raman transitions between the even-n levels within the same hyperfine state. The interaction can also be thought of as a parametric drive induced by an optical dipole force modulated at 2ω [19]. The squeeze parameter β (defined as the factor by which the variance of the squeezed quadrature is decreased) grows exponentially with the driving time. Figure 6 shows $P_{\downarrow}(t)$ for a squeezed state prepared in this way. The data are fitted to a vacuum squeezed state distribution, allowing only β to vary. The fit of the data in figure 6 demonstrates consistency with a squeezed state and gives $\beta = 40 \pm 10$ (16 dB below the zero point variance), which corresponds to $\bar{n} \approx 7.1$.

The probability distribution for a vacuum squeezed state is restricted to the even states, $P_{2n} = N(2n)!(\tanh r)^{2n}/(2^n n!)^2$, with $\beta = \exp(2r)$. The distribution is very flat; for example, with $\beta = 40$, 16%of the population is in states above $n = 20$. The Rabi frequency differences of these high-n levels are small (see figure 2(*b*)),

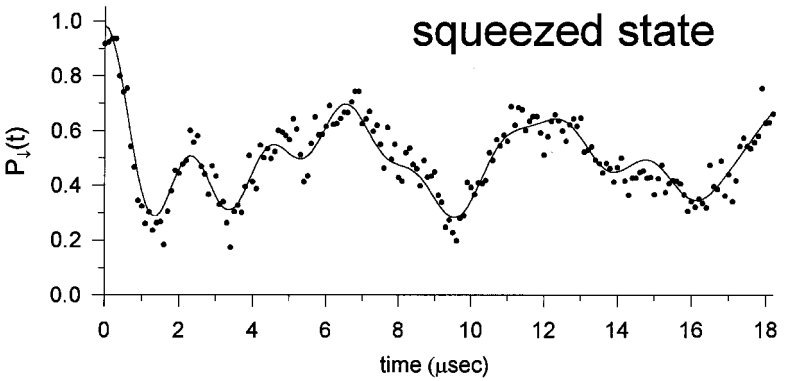

Figure 6. $P_{\downarrow}(t)$ for a squeezed state. The data are fitted to a squeezed state population distribution, yielding $\beta \approx 40 \pm 10$ (16 dB below the zero point variance), which corresponds to $\bar{n} \approx 7{\cdot}1$.

and with $\eta = 0{\cdot}202$ the Rabi frequencies begin to decrease with n after $n = 20$. The levels can no longer be well distinguished by frequency to extract the level populations.

In the above cases, we have checked our state creation through the values of the P_n. This information is, of course, incomplete since it does not reveal the coherences. Measurements completely characterizing the quantum state will be discussed below.

4.5. *A 'Schrödinger cat' state of motion*

A 'Schrödinger cat' state can be taken as a superposition of classical-like states. In Schrödinger's original thought experiment [25] he describes how we could in principle transform a superposition inside an atom to a large-scale superposition of a live and dead cat. In our experiment [26], we construct an analogous state at the single atom level. A superposition of internal states ($|\uparrow\rangle$ and $|\downarrow\rangle$) is transformed into a superposition of coherent motional states with different phases. The coherent states of the superposition are separated in space by mesoscopic distances much greater than the size of the atom.

This situation is interesting from the point of view of the quantum measurement problem associated with 'wavefunction collapse,' historically debated by Einstein and N. Bohr, among others [27]. One practical approach toward resolving this controversy is the introduction of quantum decoherence, or the environmentally induced reduction of quantum superpositions to statistical mixtures and classical behaviour [28]. Decoherence is commonly interpreted as a way of quantifying the elusive boundary between classical and quantum worlds, and almost always precludes the existence of macroscopic Schrödinger cat states, except at extremely short time scales [28]. The creation of mesoscopic Schrödinger cat states may allow controlled studies of quantum decoherence and the quantum/classical boundary.

In the present work, we create a Schrödinger cat state of the harmonic oscillator by forming a superposition of two coherent state wavepackets of the single trapped atom with a sequence of laser pulses. The coherent states are excited with the use of a pair of Raman laser beams as described above. The key to the

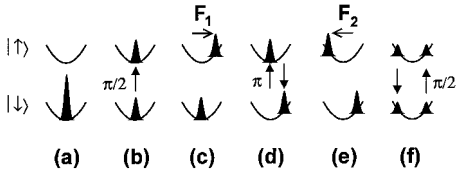

Figure 7. Evolution of the idealized position-space atomic wavepacket entangled with the internal states $|\downarrow\rangle$ and $|\uparrow\rangle$ during the creation of a 'Schrödinger cat' state with $\alpha = 3$ and $\phi = \pi$ (displacement forces in opposite directions). The wavepackets are snapshots in time, taken when the atom is at extrema of motion in the harmonic trap (represented by the parabolas). The area of the wavepackets corresponds to the probability of finding the atom in the given internal state. (*a*) The initial wavepacket corresponds to the quantum ground state of motion following laser cooling. (*b*) The wavepacket is split following a $\frac{\pi}{2}$-pulse on the carrier. (*c*) The $|\uparrow\rangle$ wavepacket is excited to a coherent state by the force $\mathbf{F}_1$ of the displacement beams. Note the force acts only on the $|\uparrow\rangle$ wavepacket, thereby entangling the internal and motional systems. (*d*) The $|\uparrow\rangle$ and the $|\downarrow\rangle$ wavepackets are exchanged, following a π-pulse on the carrier. (*e*) The $|\downarrow\rangle$ wavepacket is excited to a coherent state by the displacement beam force $\mathbf{F}_2$, which in general has a different phase with respect to the force in (*c*) ($\mathbf{F}_2 = -\mathbf{F}_1$ in the figure). The state shown in (*e*) is analogous to a 'Schrödinger cat' state. (*f*) The $|\uparrow\rangle$ and the $|\downarrow\rangle$ wavepackets are finally combined following a $\frac{\pi}{2}$-pulse on the carrier.

experiment is that the displacement beams are both polarized σ^+, so that they do not affect the $|\uparrow\rangle$ internal state. It is this selection that allows a superposition of internal states to be transformed into a superposition of motional states.

Following laser cooling to the $|\downarrow\rangle|n = 0\rangle$ state as described above, we create the Schrödinger cat state by applying several sequential pulses of the following Raman beams. (1) A $\pi/2$-pulse on the carrier splits the wavefunction into an equal superposition of states $|\downarrow\rangle|0\rangle$ and $|\uparrow\rangle|0\rangle$. (2) The displacement beams excite the motion correlated with the $|\uparrow\rangle$ component to a coherent state $|\alpha\rangle$. (3) A π-pulse on the carrier swaps the internal states of the superposition. (4) The displacement beams excite the motion correlated with the new $|\uparrow\rangle$ component to a second coherent state $|\alpha\exp(i\phi)\rangle$. (5) A final $\pi/2$-pulse on the carrier combines the two coherent states (the evolving state of the system is summarized in figure 7). The relative phases (ϕ and the phases of steps 1, 3, and 5) of the steps above are determined by the phases of the RF difference frequencies of the Raman beams, which are easily controlled by phase locking the RF sources.

The state created after step 4 is a superposition of two independent coherent states, each correlated with an internal state of the ion (i.e. for $\phi = \pi$),

$$|\Psi\rangle = (|\alpha\rangle|\uparrow\rangle + |-\alpha\rangle|\downarrow\rangle)/\sqrt{2}, \tag{9}$$

In this state, the widely separated coherent states replace the classical notions of 'dead' and 'alive' in Schrödinger's original thought experiment. We verify this mesoscopic superposition by recombining the coherent wavepackets in the final step 5. This results in an interference of the two wavepackets as the relative phase ϕ of the displacement forces (steps 2 and 4) is varied. The nature of the interference depends on the phases of steps (1), (3), and (5), and is set here to cause destructive interference of the wavepackets in the $|\downarrow\rangle$ state. We directly measure this interference by detecting the probability $P_\downarrow(\phi)$ that the ion is in the $|\downarrow\rangle$ internal state for a given value of ϕ. the signal for particular choices of the phases in 1, 3 and 5 is

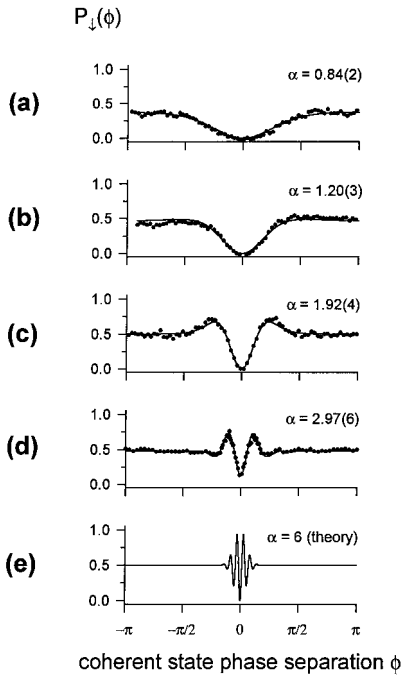

Figure 8. $P\downarrow(\phi)$ interference signal with increasing values of $|\alpha|$. The data are fitted to equation (10), yielding $\alpha = 0{\cdot}84$, $1{\cdot}20$, $1{\cdot}92$ and $2{\cdot}97$. The fit in curve (*d*) includes a term to account for the loss of contrast.

$$P\downarrow(\phi) = \tfrac{1}{2}\left[1 - C\exp\left[-\alpha^2(1 - \cos\phi)\right]\cos(\alpha^2 \sin\phi)\right], \tag{10}$$

where α is the magnitude of the coherent states and $C = 1$ is the expected visibility of the fringes in the absence of decoherence. We continuously repeat the experiment—cooling, state preparation, detection—while slowly sweeping the relative coherent state motional phase ϕ.

In figure 8, we display the measured $P\downarrow(\phi)$ for a few different values of the coherent state amplitude α, which is set by changing the duration of application of the displacement beams (steps 2 and 4 from above). The unit visibility of the interference feature near $\phi = 0$ verifies that we are producing superposition states instead of statistical mixtures, and the feature clearly narrows as α is increased. We extract the amplitude of the Schrödinger cat state by fitting the interference data to the expected form of the interference fringe. The extracted values of α agree with an independent calibration of the displacement forces. We measure coherent state amplitudes as high as $a \simeq 2{\cdot}97(6)$, corresponding to an average of $\bar{n} \simeq 9$ vibrational quanta in the state of motion. This indicates a maximum spatial separation of $4\alpha x_0 = 83(3)$ nm, which is significantly larger than the single wavepacket width characterized by $x_0 = 7{\cdot}1(1)$ nm as well as a typical atomic dimension ($\simeq 0{\cdot}1$nm). The individual wavepackets are thus clearly separated in phase space.

Of particular interest is the fact that as the separation of the cat state is made larger, the decay from superposition to statistical mixture (decoherence) becomes faster [29]. In the experiment, decoherence due to coupling to a thermal reservoir is expected to result in a loss of visibility in the interference pattern of $C = \exp(-\alpha^2\lambda t)$ where λ is the coupling constant and t the coupling time. The

exponential reduction of coherence with the square of the separation (α^2 term) undelies the reason that bigger 'cats' decay faster. In figure 8 (*d*), the observed loss of contrast at the largest observed separation may already indicate the onset of decoherence. Decoherence due to radiative coupling has been observed in cavity QED [29]. The precise control of quantum wavepackets in this version of 'Schrödinger's cat' provides a very sensitive indicator of quantum decoherence, whose characterization is of great interest to quantum measurement theory and applications such as quantum computing [30] and quantum cryptography [31].

5. Complete quantum state measurement

The controlled interaction of light and RF electromagnetic fields with the trapped atom allows us not only to prepare very general states of motion, but also to determine these quantum mechanical states using novel techniques. Few experiments have succeeded in determining the density matrices or Wigner functions of quantum systems. The angular momentum density matrices of the substate in principal quantum number $n = 3$ were measured in collisionally produced atomic hydrogen [32]; the Wigner function and density matrix of a mode of light were experimentally mapped by optical homodyne tomography [33, 34]; the Wigner function of the vibrational degree of freedom of a diatomic molecule was reconstructed with a related technique [35]; and, more recently the Wigner function of an atomic beam passing through a double slit was reconstructed [36]. Here we present the theory and experimental demonstration of two distinct schemes that allow us to reconstruct both the density matrix in the number state basis and the Wigner function of the motional state of a single trapped atom [37]. For other proposals to measure the motional state of a trapped atom, see this issue and [38, 39]. As described above, we are able to prepare a variety of non-classical input states [14] which can, for example, exhibit negative values of the Wigner function. Also, comparing the results of the state determination with the state we intended to produce can give an idea of the accuracy of the preparation.

Both of our measurement techniques rely on our ability to displace the input state to several different locations in phase space. Specifically, a coherent displacement [14, 18] $U(-\alpha) = U^{\dagger}(\alpha) = \exp(\alpha^* a - \alpha a^{\dagger})$ ($-\alpha$ is used for convenience below) controlled in phase and amplitude is used in our schemes. We then apply radiation on the blue sideband to the atom for a time t, which induces a resonant exchange between the motional and internal degrees of freedom (see section 2). For each α and time t, the population $P_{\downarrow}(t, \alpha)$ of the $|\downarrow\rangle$ level is then measured by monitoring the fluorescence produced in driving the resonant dipole cycling transition (see section 2). For these experiments the internal state at $t = 0$ is always prepared to be $|\downarrow\rangle$ for the various input states, so the signal averaged over many measurements is

$$P_{\downarrow}(t, \alpha) = \tfrac{1}{2}\left\{1 + \sum_{k=0}^{\infty} Q_k(\alpha) \cos(2\Omega_{k,k+1} t) \exp(-\gamma_k t)\right\}. \qquad (11)$$

Without the coherent displacement we would just recover the previously discussed $P_{\downarrow}(t)$ signal (equation (7)) and would find the populations of the motional eigenstates only. But since we repeat these measurements for several magnitudes

and phases of the coherent displacement, we are able to extract information about the off-diagonal elements of the density matrix and can also reconstruct the Wigner function from the measured displaced populations $Q_k(\alpha)$.

5.1. *Reconstruction of the number state density matrix*

To reconstruct the density marix ρ in the number state basis, we use the relation

$$Q_k(\alpha) = \langle k|U^\dagger(\alpha)\rho U(\alpha)|k\rangle = \langle \alpha, k|\rho|\alpha, k\rangle, \tag{12}$$

where $|\alpha, k\rangle$ is a coherently displaced number state [40]. Hence every $Q_k(\alpha)$ is the population of the displaced number state $|\alpha, k\rangle$ for an ensemble characterized by the input density matrix ρ. Rewriting (12) we get

$$\begin{aligned} Q_k(\alpha) &= \frac{1}{k!}\langle 0|a^k U^\dagger(\alpha)\rho U(\alpha)(a^\dagger)^k|0\rangle \\ &= \frac{1}{k!}\langle \alpha|(a-\alpha)^k\rho(a^\dagger-\alpha^*)^k|\alpha\rangle \\ &= \frac{\exp(-|\alpha|^2)|\alpha|^{2k}}{k!}\sum_{n,m=0}^{\infty}\sum_{j,j'=0}^{k}\frac{(\alpha^*)^{n-j}\alpha^{m-j'}}{n!m!} \\ &\quad\times(-1)^{-j-j'}\begin{bmatrix}k\\ j\end{bmatrix}\begin{bmatrix}k\\ j'\end{bmatrix}[(m+j)!(n+j')!]^{\frac{1}{2}}\rho_{n+j',m+j}. \end{aligned} \tag{13}$$

To separate the contributions of different matrix-elements $\rho_{n,m}$, we may displace the state along a circle,

$$\alpha_p = |\alpha|\exp[i(\pi/N)p], \tag{14}$$

where $p \in \{-N, \ldots, N-1\}$. The number of angles $2N$ on that circle determines the maximum number of states $n_{\max} = N-1$ that can be included in the reconstruction. With a full set of populations of the state displaced along $2N$ points on a circle we can perform a discrete Fournier transform of equation (14) evaluated at the values α_p, and we obtain the matrix equations

$$\begin{aligned} Q_k^{(l)} &\equiv \frac{1}{2N}\sum_{p=-N}^{N-1}Q_k(\alpha_p)\exp[-il(\pi/N)p] \\ &= \sum_{n=\max(0,-l)}^{\infty}\gamma_{kn}^{(l)}\rho_{n,n+l}, \end{aligned} \tag{15}$$

with matrix elements

$$\begin{aligned} \gamma_{kn}^{(l)} &= \frac{\exp(-|\alpha|^2)|\alpha|^{2k}}{k!}\sum_{j=0}^{\min(k,n)}\sum_{j'=0}^{\min(k,l+n)}|\alpha|^{2(n-j-j')+l} \\ &\quad\times(-1)^{-j-j'}\begin{bmatrix}k\\ j\end{bmatrix}\begin{bmatrix}k\\ j'\end{bmatrix}\frac{[(l+n)!n!]^{\frac{1}{2}}}{(l+n-j)!(n-j')!} \end{aligned} \tag{16}$$

for every diagonal $\rho_{n,n+l}$ of the density matrix. To keep the matrix dimension finite, a cutoff for the maximum n in (15) is introduced, based on the magnitude of the

input state. For an unknown input state an upper bound on n may be extracted from the populations $Q_k(\alpha)$. If these are negligible for k higher than a certain $k_{\max}$ and all displacements α, they are negligible in the input state as well, and it is convenient to truncate equation (15) at $n_{\max} = k_{\max}$. The resulting matrix equation is overcomplete for some l, but the diagonals $\rho_{n,n+l}$ can still be reconstructed by a general linear least squares method [16].

5.2. *Reconstruction of s-parameterized quasiprobability distributions*

As pointed out by several authors, s-parametrized quasiprobability distributions $F(\alpha, s)$ have a particularly simple representation when expressed in populations of displaced number states $Q_k(\alpha)$ [40, 41, 42, 43].

$$F(\alpha, s) = \frac{1}{\pi}\sum_{n=0}^{\infty}\left[\frac{s+1}{2}\right]^n \sum_{k=0}^{n}(-1)^k\binom{n}{k}Q_k(\alpha). \tag{17}$$

For $s = -1$ the sum breaks down to one term and $F(\alpha, -1) = Q_0(\alpha)/\pi$ gives the value of the Q quasi-probability distribution at the complex coordinate α [44]. Also, for $s = 0$, the Wigner function $F(\alpha, 0) = W(\alpha)$ for every point α in the complex plane can be determined by the single sum

$$W(\alpha) = \frac{2}{\pi}\sum_{n=0}^{\infty}(-1)^n Q_n(\alpha). \tag{18}$$

In our reconstruction, the sum is carried out only to a finite $n_{\max}$, as described above. Since truncation of the sum leads to artifacts in the quasi-probability distributions [45], we have averaged our experimental data over different $n_{\max}$. This smoothes out the artifacts to a high degree.

In contrast to the density matrix method described in section 5.1, summing the displaced probabilities with their weight factors provides a direct method to obtain the quasi-probability distribution at the point α in phase space, without the need to measure at other values of α. This also distinguishes the method from preceding experiments that determined the Wigner function by inversion of integral equations (tomography) [33, 35].

5.3. *Experimental results*

The coherent displacement needed for the reconstruction mapping is provided by a spatially uniform classical driving field at the trap oscillation frequency. This field is applied on one of the trap compensation electrodes [9] for a time of about 10 μs. The RF oscillators that create and displace the state are phase locked to control their relative phase. Different displacements are realized by varying the amplitude and the phase of the displacement oscillator. For every displacement α, we record $P_\downarrow(t, \alpha)$. $Q_n(\alpha)$ can be found from the measured traces with a singular value decomposition (see section 4.2). To determine the amplitude $|\alpha|$ of each displacement, the same driving field is applied to the $|n = 0\rangle$ ground state and the resulting collapse and revival trace is fitted to that of a coherent state (see section 4.3).

The accuracy of the reconstruction is limited by the uncertainty in the applied displacements, the errors in the determination of the displaced populations, and decoherence during the measurement. The value of the Wigner function is found

by a sum with simple error propagation rules. The density matrix is reconstructed by a linear least-squares method) and it is straightforward to calculate a covariance matrix [16]. As the size of the input state increases, decoherence and the relative accuracy of the displacements become more critical, thereby increasing their uncertainties.

In figure 9, we show the reconstruction of both the number state density matrix (*a*) and surface and contour plots of the Wigner function (*b*) of an approximate $|n = 1\rangle$ number state. The plotted surface is the result of fitting a linear interpolation between the actual data points to a 0·1 grid. The octagonal shape is an artifact of the eight measured phases per radius. The white contour represents $W(\alpha) = 0$. The negative values around the origin highlight the non-classical character of this state. The Wigner function $W(\alpha)$ is rotationally symmetric within the experimental errors as confirmed by our measured values. Therefore we averaged sets of data with the same value of $|\alpha|$. The averaged points are displayed in figure 9 (*c*), together with a radial slice through the theoretical Wigner function for a pure number state (dashed line) and a thermally contaminated state (solid line) assuming the ion is prepared in a thermal distribution with a probability of finding it in ground state of only ≈90% after cooling and prior to the preparation of the $|n = 1\rangle$ number state. This was independently verified to be the case in our experiment by comparing the magnitude of red and blue sidebands after Raman-sideband cooling to the ground state [10]. Again the large negative part of the Wigner function around the origin highlights the fact that the prepared state is non-classical.

In contrast to the number state, the state closest to a classical state of motion in a harmonic oscillator is a coherent state. As one example, we have excited and reconstructed a small coherent state with amplitude $|\beta| \approx 0{\cdot}67$. The experimental amplitude and phase of the number state density matrix are depicted in figure 10. The off-diagonal elements are generally slightly smaller for the experiment than we would expect from the theory of a pure coherent state. In part this is due to decoherence during the measurement, so the reconstruction shows a mixed state character rather than a pure coherent state signature. This view is further supported by the fact that farther off-diagonal elements seem to decrease faster than direct neighbours of the diagonal.

The reconstructed Wigner function of a second coherent state with amplitude $|\beta| \approx 1.5$ is shown in figure 11. The plotted surface is the result of fitting a linear interpolation between the actual data points to a 0·13 by 0·13 grid. The approximately Gaussian minimum uncertainty wavepacket is centred around a coherent amplitude of about 1·5 from the origin. The half-width at half maximum is about 0·6, in accordance with the minimum uncertainty half-width of $\left[\ln(2)/2\right]^{\frac{1}{2}} \approx 0{\cdot}59$. To suppress truncation artifacts in the Wigner function summation (18) [45], we have averaged over $n_{\max} = 5$ and $n_{\max} = 6$.

We have also created a coherent superposition of $|n = 0\rangle$ and $|n = 2\rangle$ number states. This state is ideally suited to demonstrate the sensitivity of the reconstruction to coherences. the only non-zero off-diagonal elements should be ρ_{02} and ρ_{20}, with a magnitude of $|\rho_{02}| = |\rho_{20}| = \left[\rho_{00}\rho_{22}\right]^{\frac{1}{2}} \approx 0.5$ for a superposition with about equal probability of being measured in the $|n = 0\rangle$ or $|n = 2\rangle$ state. In the reconstruction shown in figure 12 the populations ρ_{00} and ρ_{22} are somewhat smaller, due to imperfections in the preparation, but the coherence has the expected value of $|\rho_{20} = |\rho_{02}| \approx \left[\rho_{00}\rho_{22}\right]^{\frac{1}{2}}$.

For a known density matrix one can also find the Wigner function by

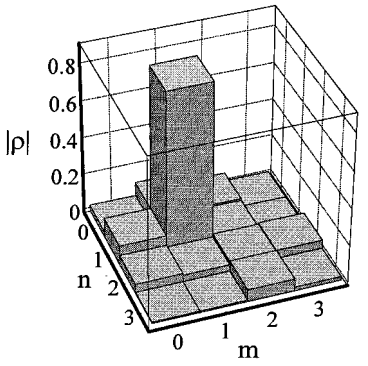

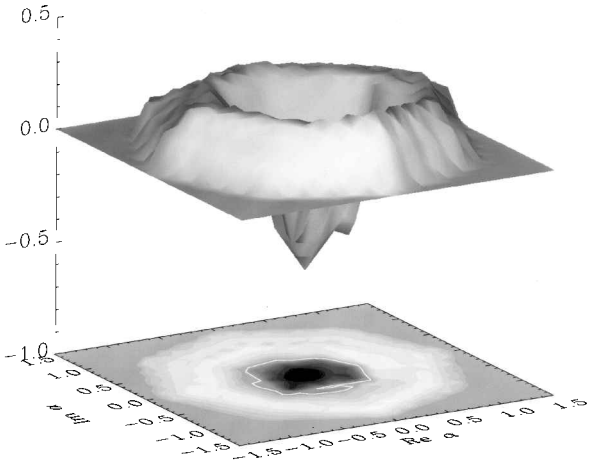

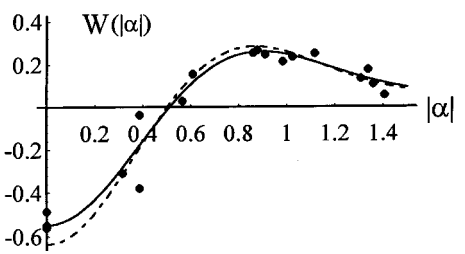

Figure 9. (*a*) reconstructed number state density matrix amplitudes ρ_{nm} for an approximate $|n = 1\rangle$ number state. The coherent reconstruction displacement amplitude was $|\alpha| = 1{\cdot}15(3)$. The number of relative phases $N = 4$ in equation (14), so $n_{\max} = 3$. (*b*) Surface and contour plots of the Wigner function $W(\alpha)$ of the $|n = 1\rangle$ number state. The white contour represents $W(\alpha) = 0$. The negative values around the origin highlight the non-classical character of this state. (*c*) The Wigner function of the $|n = 1\rangle$ number state is rotationally symmetric: $W(\alpha) = W(|\alpha|)$. In this figure we show a radial slice through this function for a pure number state (dashed line) and a thermally contaminated state (solid line) which assumes the ion is in the ground state only ≈90% of the time after cooling. This was independently verified after sideband cooling [10]. The dots are experimentally determined values of the Wigner function, averaged for equal $|\alpha|$.

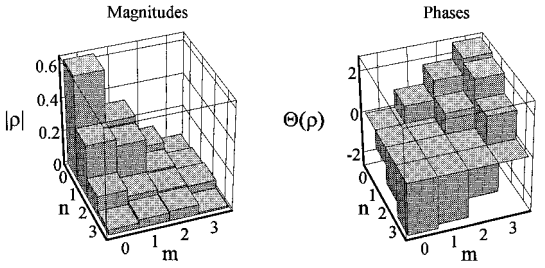

Figure 10. Experimental amplitudes ρ_{nm} and phases $\Theta(\rho_{nm})$ of the number state density matrix elements of a $|\beta| \approx 0{\cdot}67$ coherent state. The state was displaced by $|\alpha| \approx 0.92$, for $N = 4$ in equation (14).

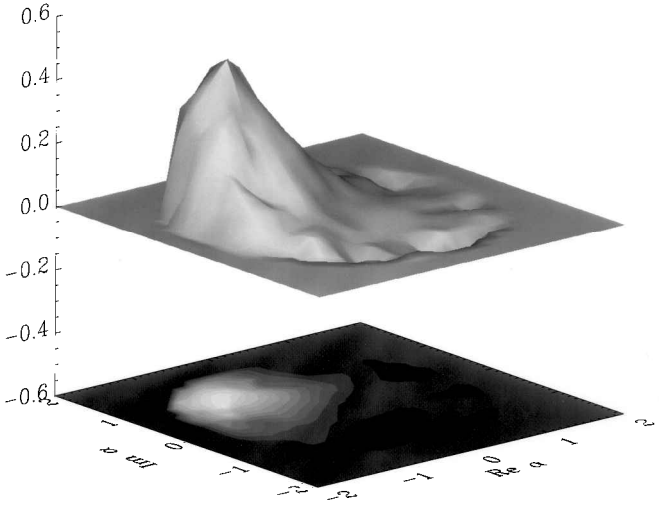

Figure 11. Surface and contour plots of the reconstructed Wigner function of a coherent state. The approximately Gaussian minimum uncertainty wavepacket is centred around a coherent amplitude of about 1·5 from the origin. The half-width at half maximum is about 0·6, in accordance with the minimum uncertainty half-width of $\left[\ln(2)/2\right] \approx 0{\cdot}59$.

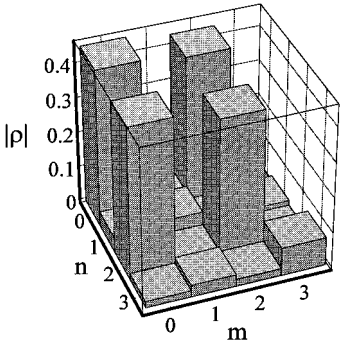

Figure 12. Reconstructed density matrix amplitudes of an approximate $1/\sqrt{2}(|n = 0\rangle - i|n = 2\rangle)$ state. The state was displaced by $|\alpha| = 0{\cdot}79$ for $N = 4$ in equation (14). The amplitudes of the coherences indicate that the reconstructed density matrix is close to that of a pure state.

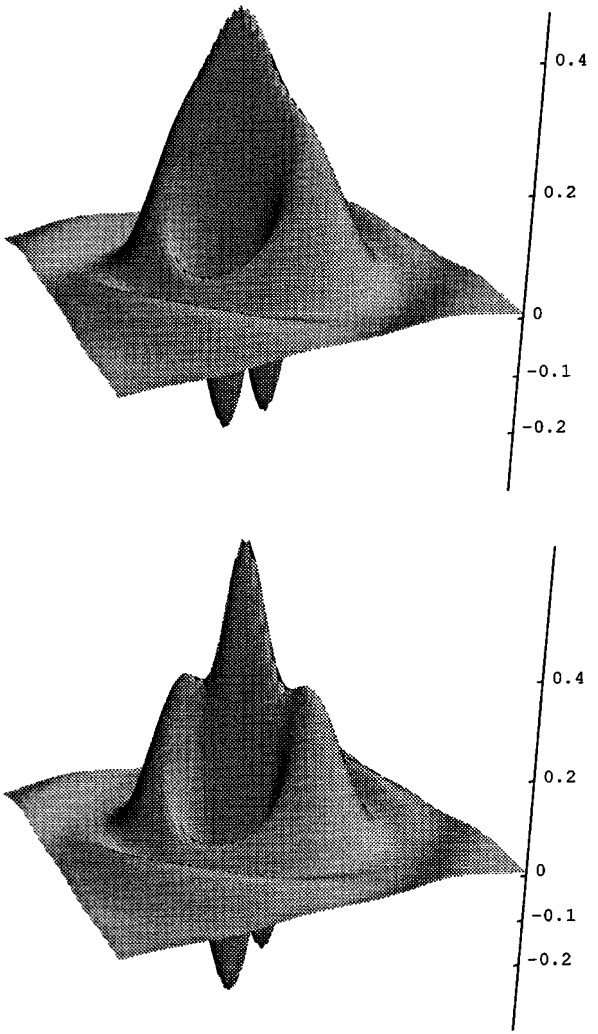

Figure 13. Comparison of the Wigner function of an approximate $1/\sqrt{2}(|n=0\rangle - i|n=2\rangle)$ state transformed from our experimental density matrix data (*a*) with its theoretical counterpart (*b*).

expanding equation (18) in the number state basis,

$$W(\alpha) = \frac{2}{\pi}\sum_{n=0}^{\infty}(-1)^n \sum_{k,l=0}^{\infty}\langle\alpha, n|k\rangle\rho_{kl}\langle l|\alpha, n\rangle, \tag{19}$$

with the matrix elements given by ($l \geqslant n$) [46]

$$\langle l|\alpha, n\rangle = \left[n!/l!\right]^{\frac{1}{2}}\alpha^{l-n}\exp(-1/2|\alpha|^2)\mathcal{L}_n^{(l-n)}(|\alpha|^2), \tag{20}$$

where $\mathcal{L}_n^{(l-n)}$ is a generalized Laguerre polynomial. Using this approach we have generated a plot of the Wigner function using our density matrix data. The result is shown in figure 13 together with the theoretical Wigner function for a $1/\sqrt{2}(|n=0\rangle - i|n=2\rangle)$ state. The differences can be traced to the imperfections

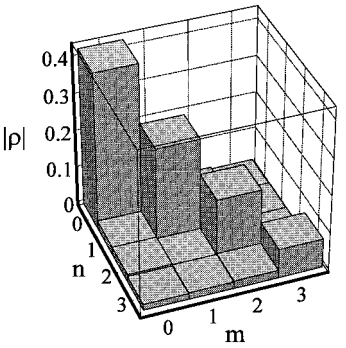

Figure 14. Reconstructed density matrix of an $\bar{n} \approx 1.3$ thermal state. This state was displaced by $|\alpha| = 0{\cdot}78$, for $N = 4$ equation (14). As one would expect for a thermal state, no coherences are present within the experimental uncertainties and the populations drop exponentially for higher n.

in the preparation also visible in figure 12; the small but non-zero values of $|\rho_{11}|$ and $|\rho_{33}|$ and the respective coherences lead to the differences in the central feature of the Wigner function.

Finally, we have generated a thermal state by only Doppler-cooling the ion. The reconstruction of the resulting state is depicted in figure 14. As expected, there are no coherences, and the diagonal, which gives the number state occupation, shows an exponential behaviour within the experimental errors, indicating a mean occupation number $\bar{n} \approx 1{\cdot}3$.

6. Conclusions

The interaction of a trapped atom with classical light fields can lead to experimental situations that allow us to coherently prepare a multitude of quantum states, both classical-like and non-classical in character. Since the interaction can be tailored to resemble the Jaynes-Cummings model, the system is suited to realizing many proposals originally introduced in the realm of quantum optics and cavity quantum electrodynamics. One special application is the preparation of a state where the internal degree of freedom is entangled with two coherent states, with a separation in phase space much bigger than their spread. This state, bearing many features of 'Schrödinger's cat', is well suited for the study of decoherence phenomena on the boundary of quantum and classical mechanics such as the decoherence of mesoscopic objects. Such studies are especially interesting in our system since we should be able to engineer different couplings and reservoirs by an appropriate choice of the interaction Hamiltonian [47].

Our level of control in the preparation of the states also allows us to prepare the same state many times to a high accuracy. By extending our techniques to several simultaneously trapped ions, we should be able to controllably prepare and manipulate their combined state and thus implement simple quantum logic gates [48, 49]. The techniques described here for characterizing the quantum state of motion, combined with a Ramsey-type spectroscopy on the internal states, seem to lead to a method for completely measuring the internal and motional states of several simultaneously trapped ions (for an alternative method see [50]). Apart

from detecting quantum correlations in these states, this might be a useful way to fully characterize simple quantum logic gates [51].

Acknowledgments

This work is supported by the United States National Security Agency, the Office of Naval Research and the Army Research Office. D.L. gratefully acknowledges a deutsche Forschungsgemeinschaft research grant. D.M.M. is supported by an N.R.C. postdoctoral fellowship. We thank W. Vogel, M. Collet, P. Knight, J. I. Cirac and P. Zoller for stimulating discussions. We acknowledge important contributions by J. Bergquist and helpful comments on the manuscript by M. Young, B. Esry and B. Jelenkovic.

References

[1] Jaynes, E. T., and Cummings, F. W., 1963, *Proc. IEEE,* **51,** 89.
[2] Shore, B. W., and Knight, P. L., 1993, *J. Mod. Opt.,* **40,** 1195.
[3] Blockley, C. A., Walls, D. F., and Risken, H., 1992, *Europhys. Lett.,* **17,** 509.
[4] Cirac, J. I., Blatt, R., Parkins, A. S., and Zoller, P., 1993, *Phys. Rev. Lett.*, **70,** 762.
[5] Paul, W., 1990, *Rev. Mod. Phys.*, **62,** 531.
[6] Glauber, R. J., 1992, *Laser Manipulation of Atoms and Ions*, Proc. Int. School of Physics 'Enrico Fermi' Course 118, edited by E. Arimondo *et al.*, (Amsterdam: North Holland), p. 643.
[7] Bardroff, P. J., Leichtle, C., Schrade, G., and Schleich, W. P., 1996, *Act. Phys. Slov.,* **46,** 1.
[8] Cirac, J. I., Garay, L. J., Blatt, R., Parkins, A. S., and Zoller, P., 1994, *Phys. Rev.* A, **49,** 421.
[9] Jefferts, S., Monroe, C., Bell, E., and Wineland, D. J., 1994, *Phys. Rev.* A, **51,** 3112.
[10] Monroe, C., Meekhof, D. M., King, B. E., Jefferts, S. R., Itano, W. M., Wineland, D. J., and Gould, P. L., 1995, *Phys. Rev. Lett.*, **75,** 4011.
[11] Eschner, J., Appasamy, B., and Toschek, P. E., 1995, *Phys. Rev. Lett.*, **74,** 2435.
[12] Cirac, J. I., Blatt, R., and Zoller, P., 1994, *Phys. Rev.* A, **49,** R3174.
[13] Blatt, R., Cirac, J. I., and Zoller, P., 1995, *Phys. Rev.* A, **52,** 518.
[14] Meekhof, D. M., Monroe, C., King, B. E., Itano, W. M., and Wineland, D. J., 1996, *Phys. Rev. Lett.*, **76,** 1796; 1996, erratum, *ibid.*, **77,** 2346.
[15] Stenholm, S., 1986, *Rev. Mod. Phys.*, **58,** 699.
[16] Press, W. H., Teukolsky, S. A., Vetterling, W. T., and Flannery, B. P., 1992, *Numerical Recipes* (Cambridge University Press).
[17] von Foerster, T., 1975, *J. Phys.* A, **8,** 95; Eberly, J. H., Narozhny, N. B., and Sanchez-Mondragon, J. J., 1980, *Phys. Rev. Lett.*, **44,** 1323.
[18] Carruthers, P., and Nieto, M. M., 1965, *Am. J. Phys.*, **7,** 537.
[19] Wineland, D. J., Bergquist, J. C., Bollinger, J. J., Itano, W. M., Moore, F. L., Gilligan, J. M., Raizen, M. G., Heinzen, D. J., Weimer, C. S., and Manney, C. H., 1992, *Laser Manipulation of Atoms and Ions*, Proc. Int. School of Physics 'Enrico Fermi' Course 118, edited by E. Arimondo *et al.* (Amsterdam: North Holland), p. 553.
[20] Cirac, J. I., Parkins, A. S., Blatt, R., and Zoller, P., 1993, *Phys. Rev. Lett.*, **70,** 556.
[21] Janszky, J., and Yushin, Y. Y., 1986, *Opt. Comm.*, **59,** 151; Fan Hong Yi and Zaidi, H. R., 1988, *Phys. Rev.* A, **37,** 2985; Heinzen, D. J., and Wineland, D. J., 1990, *Phys. Rev.* A, **42,** 2977.
[22] Brune, M., Schmidt-Kaler, F., Maali, A., Dreyer, J., Hagley, E., Raimond, J. M., and Haroche, S., 1996, *Phys. Rev. Lett.*, **76,** 1800.
[23] Buck, B., Sukumar, C. V., 1981, *Phys. Lett.* A, **81,** 132.
[24] Knight, P., 1986, *Phys. Scr.* T, **12,** 51.
[25] Schrödinger, E., 1935, *Naturwissenschaften*, **23,** 807.

[26] Monroe, C., Meekhof, D. M., King, B. E., and Wineland, D. J., 1996, *Science*, **272,** 1131.
[27] Wheeler, J. A., and Zurek, W. H. (editors), 1983, *Quantum Theory and Measurement* (Princeton NJ: Princeton Univ. Press).
[28] Zurek, W. H., 1991, *Phys. Today*, **44,** 36.
[29] Brune, M., Hagley, E., Dreyer, J., Maitre, X., Maali, A., Wunderlich, C., Raimond, J. M., and Haroche, S., 1996, *Phys. Rev. Lett.*, **77,** 4887.
[30] Ekert, A., and Josza, R., 1966, *Rev. Mod. Phys.*, **68,** 733.
[31] Bennett, C. H., 1996, *Phys. Today*, **48,** 24.
[32] Ashburn, J. R., Cline, R. A., van der Burgt, P. J. M., Westerveldt, W. B., and Risley, J. S., 1990, *Phys. Rev.* A, **41,** 2407.
[33] Smithey, D. T., Beck, M., Raymer, M. G., and Faridani, A., 1993, *Phys. Rev. Lett.*, **70,** 1244.
[34] Breitenbach, G., Möller, T., Pereira, S. F., Poizat, J. Ph., Schiller, S., and Mlynek, J., 1995, *Opt. Soc.* B, **12,** 2304.
[35] Dunn, T. J., Walmsley, I. A., and Mukamel, S., 1995, *Phys. rev. Lett.*, **74,** 884.
[36] Kurtsiefer, C., and Mlynek, J., 1997, *Nature*, **386,** 150.
[37] Leibfried, D., Meekhof, D. M., King, B. E., Monroe, C. M., Itano, W. M., Wineland, D. J., 1996, *Phys. Rev. Lett.*, **77,** 4281.
[38] Wallentowitz, S., and Vogel, W., 1995, *Phys. Rev. Lett.*, **75,** 2932; Poyatos, J. F., Walser, R., Cirac, J. I., Zoller, P., and Blatt, R., 1996, *Phys. Rev.* A, **53,** R1966.
[39] D'Helon, C., and Milburn, G. J., 1996, *Phys. Rev.* A, **54,** R25; Bardroff, P. J., Leichtle, C., Schrade, G., and Schleich, W. P., 1996, *Phys. Rev. Lett.*, **77,** 2198.
[40] Moya-Cessa, H., and Knight, P. L., 1993, *Phys. Rev.* A, **48,** 2479.
[41] Royer, A., 1985, *Phys. Rev. Lett.*, **55,** 2745.
[42] Wallentowitz, S., and Vogel, W., 1996, *Phys. Rev.* A, **53,** 4528.
[43] Banaszek, K., and Wodkiewicz, K., 1996, *Phys. Rev. Lett.*, **76,** 4344.
[44] Poyatos, J. F., Walser, R., Cirac, J. I., Zoller, P., and Blatt, R., 1996, *Phys. Rev.* A, **53,** R1966.
[45] Collett, M., and Walls, D., private communication, July 1996; see also Banaszek, K., and Wodkiewicz, K., this issue, 2441.
[46] Cahill, K. E., Glauber, R. J., 1969, *Phys. Rev.*, **177,** 1857.
[47] Poyatos, J. F., Cirac, J. I., and Zoller, P., 1996, *Phys. Rev. Lett.*, **77,** 4728.
[48] Cirac, J. I., and Zoller, P., 1995, *Phys. Rev. Lett.*, **74,** 4091.
[49] Monroe, C., Meekhof, D. M., King, B. E., Itano, W. M., and Wineland, D. J., 1995, *Phys. Rev. Lett.*, **75,** 4714.
[50] Wallentowitz, S., de Mathos Filho, R., and Vogel, W., Sept. 1996, preprint.
[51] Poyatos, J. F., Cirac, J. I., and Zoller, P., 1997, *Phys. Rev. Lett.*, **78,** 390.